THE JOURNAL OF PHYSICAL CHEMISTRY LETTERS
A JOURNAL OF THE AMERICAN CHEMICAL SOCIETY

pubs.acs.org/JPCL

Letter

Transport Modeling of Locally Photogenerated Excitons in Halide Perovskites

Kuen Wai Tang, Senlei Li, Spencer Weeden, Ziyi Song, Luke McClintock, Rui Xiao, R. Tugrul Senger, and Dong Yu*

Cite This: J. Phys. Chem. Lett. 2021, 12, 3951−3959

Read Online

ACCESS | Metrics & More | Article Recommendations | Supporting Information

ABSTRACT: Excitons have fundamental impacts on optoelectronic properties of semiconductors. Halide perovskites, with long carrier lifetimes and ionic crystal structures, may support highly mobile excitons because the dipolar nature of excitons suppresses phonon scattering. Inspired by recent experimental progress, we perform device modeling to rigorously analyze exciton formation and transport in methylammonium lead triiodide under local photoexcitation by using a finite element method. Mobile excitons, coexisting with free carriers, can dominate photocurrent generation at low temperatures. The simulation results are in excellent agreement with the experimentally observed strong temperature and gate dependence of carrier diffusion. This work signifies that efficient exciton transport can substantially influence charge transport in the family of perovskite materials.

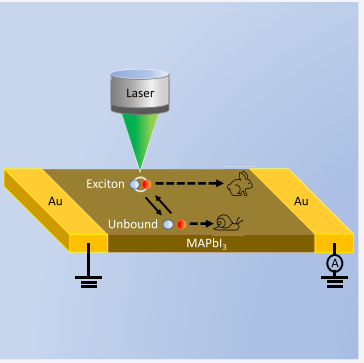

Excitons, electron−hole pairs bound by Coulomb interaction, not only strongly influence the optical properties of semiconducting materials by creating resonant optical absorption but also play a crucial role in electronic properties such as how photoexcited carriers are transported in the materials. Furthermore, fundamental research on excitons has revealed fascinating and rich physics. Excitons can form more complicated quasi-particles such as trions, biexcitons,[1,2] exciton polarons,[3] and exciton polaritons.[4] Excitons may undergo a gas−liquid phase transition[5] and condense into an electronic insulator or a superfluidic quantum state.[6,7] How excitons interact with free carriers and phonons is essential to understanding these exotic behaviors. For example, in wide-bandgap semiconductors with low dielectric constants, excitons heavily dressed with phonons can be immobilized by a self-trapping mechanism, such as in the case of metal halides and one-dimensional (1D) hybrid halide perovskites.[8,9] However, in inorganic semiconductors with larger dielectric constants, electric field screening can result in highly mobile excitons, exhibiting mobilities as high as 2×10^6 cm^2 V^{-1} s^{-1} at 1.5 K in Si.[10]

Hybrid halide perovskites show unique properties that facilitate unprecedented rapid development in optoelectronic applications such as solar cells and light-emitting devices. Halide perovskites have been shown to have a soft lattice with Young's moduli approximately 10 times lower than those of common inorganic semiconductors.[11] As a result of the highly polarizable lattice, a charge carrier can effectively form a large polaron with a diameter much larger than the unit cell size.[12] Large polarons in halide perovskites may account for the unique optoelectronic properties of the materials, including electric field screening, defect tolerance, slow hot carrier cooling, and moderate charge carrier mobility.[13,14] Analogous to charged (electron or hole) polarons, excitons may interact with the crystal lattice and form polaronic excitons. The phonon scattering of exciton polarons is fundamentally different from that of charged polarons and is poorly understood. The carrier scattering is expected to be dominated by longitudinal optical (LO) phonons in halide perovskites.[15]

We recently proposed that the phonon scattering rate of excitons can be significantly suppressed compared to that of free carriers and charged polarons, because the electric field created by a dipole is shorter-range than the monopolar field.[16] Briefly, the interaction of an exciton with LO phonons can be modeled through its induced dipole moment, expressed like the polarizability of a hydrogen atom, $\alpha = 9a_{ex}^3/2$, where a_{ex} is the exciton Bohr radius.[17] The interplay between the excitonic and polaronic effects in halide perovskites is highly elaborate and has been a subject of debate in the literature in various forms. Halide perovskites are highly polar materials with significantly different values of optical and static dielectric constants, and they have lower phonon energies due to their softness. These two properties combine to lead to high

Received: February 15, 2021
Accepted: April 14, 2021
Published: April 19, 2021

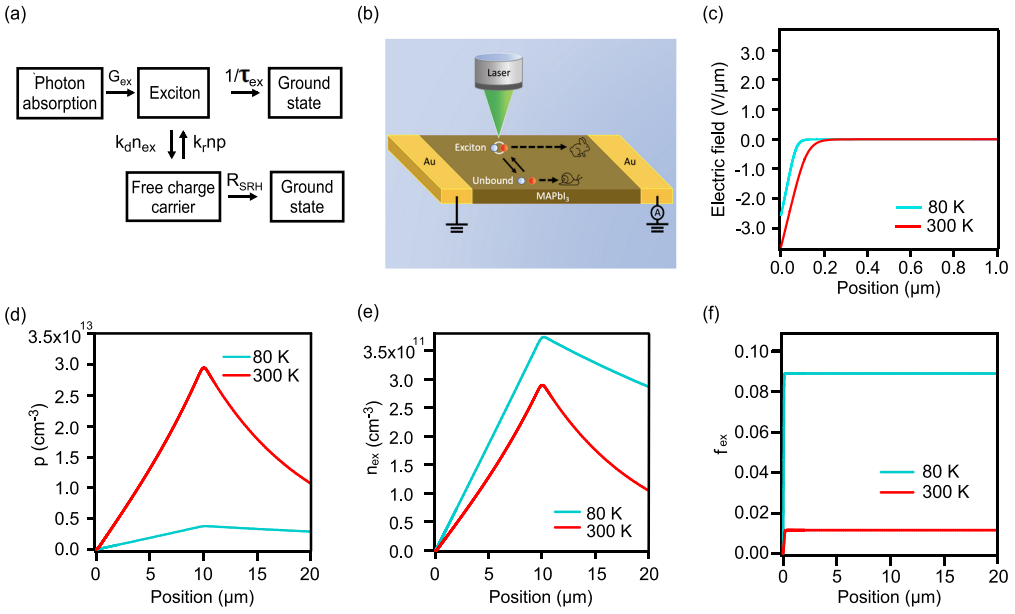

Figure 1. Simulated distributions of the electric field, free carriers and excitons, under point excitation at x = 10 μm with a power P = 1 nW and V_{sd} = 0 V in a $MAPbI_3$ nanoribbon device. (a) Diagram showing the generation, pairing/dissociation, and recombination processes of coexisting excitons and free carriers. (b) Schematic drawing of the device configuration under a focused laser and the generation and transport of excitons and free carriers. (c–f) Distribution of the electric field, free hole density, exciton density, and exciton fraction, respectively, at 80 and 300 K. E_b is set to 10 meV at 300 K and 20 meV at 80 K for all plots. This figure shows the distributions near the contact. The distributions over the entire channel are shown in Figure S3.

Fröhlich coupling constants for the charge–phonon interactions. Therefore, the simple hydrogenic model of excitons does not apply well in these materials. To characterize the excitons, we use exciton size and binding energy values as calculated using an effective interaction potential model for polaronic excitons.[18,19] In this model, the rate of scattering of an exciton from LO phonons is reduced by a factor of $\gamma = \left(\frac{9a_{ex}^3 R_h}{2\epsilon_\infty R_{ex}^4}\right)^2$ compared to a hole. Here, R_h and R_{ex} are the hole and exciton polaron radii, respectively, where the polaron radius of a quasi-particle of mass m interacting with LO phonons is given by $R = \sqrt{\frac{\hbar}{2m\omega_{LO}}}$. We have estimated that $\gamma \approx 10^{-3}$, indicating exciton mobility is significantly higher than that of free carriers or charged polarons.[16]

This theoretical prediction is supported by our experimental observation of the strong temperature dependence of photogenerated carrier diffusion in single-crystal methylammonium lead triiodide ($MAPbI_3$) microstuctures, by scanning photocurrent microscopy (SPCM).[16] Carrier diffusion lengths were found to increase much more rapidly than expected from phonon scattering of charged polarons as the temperature decreased. Instead, the experimental results can be understood by the exponentially increased fraction of highly mobile excitons at low temperatures. Furthermore, carrier diffusion lengths were found to increase by a factor of 8 with an increase in majority carrier (electron) concentration under the gate voltage (V_G). This is also consistent with the exciton model, as the higher carrier concentration increases the probability of exciton formation,[20] leading to a larger exciton fraction and hence a higher effective mobility.

Here, inspired by the previous experimental work, we perform device modeling and numerical simulations to rigorously analyze the exciton formation and transport in $MAPbI_3$ microstructures under local photoexcitation. The simulation results agree well with our experimental observations, including temperature and gate-dependent photocurrent decay lengths. A similar approach[21] has been applied to simulate the excitonic effects in conducting polymer solar cells, but excitons were treated as immobile particles. In this Letter, we instead consider that excitons are significantly more mobile than free carriers. Another major difference is that the device geometry examined in the previous work was a solar cell under uniform illumination, while we consider a point photoexcitation as used in SPCM. SPCM is a powerful experimental technique that provides spatially resolved photocurrent mapping and insights into carrier transport.[22−24] In particular, this method has been recently applied to extract carrier diffusion length, a crucial optoelectronic parameter in halide perovskites.[16,25−27] However, these previous SPCM efforts have considered only free carriers, ignoring the contribution of excitons. We show that excitons can actually dictate the photocurrent distributions at low temperatures.

We consider three types of coexisting particles in the material under light illumination: free electron, free hole, and exciton. To be clear, by "free" we mean the electron and hole are not bound to an exciton, but they may still be dressed by phonons, resulting in reduced mobilities. A free electron and a free hole are bound to an exciton at a rate described by Langevin recombination (k_r), which assumes an exciton forms once an electron and a hole move within their joint capture radius[28]

$$k_r = \frac{\mu e}{\epsilon_r \epsilon_0} \tag{1}$$

where $\mu = \mu_n + \mu_p$ is the sum of electron and hole mobilities and ϵ_r is the dielectric constant. An exciton can also dissociate

https://doi.org/10.1021/acs.jpclett.1c00507
J. Phys. Chem. Lett. 2021, 12, 3951−3959

into a free electron and a free hole at a rate that depends on local electric field E

$$k_d(E) = k_r K(E) \tag{2}$$

At $E = 0$, the equilibrium constant of exciton dissociation $K(0)$ is given by[29]

$$K(0) = \frac{3}{4\pi {a_{ex}}^3} e^{-E_b/k_B T} \tag{3}$$

where a_{ex} is the exciton size and $E_b = \frac{e^2}{4\pi\varepsilon_r\varepsilon_0 a}$ is the exciton binding energy. In the presence of an electric field, excitons dissociate at a higher rate given by[28]

$$K(E)/K(0) = \frac{J_1(2\sqrt{-2b})}{\sqrt{-2b}} \tag{4}$$

where J_1 is the Bessel function of order one and $b = \frac{e^3 E}{8\pi\varepsilon_r\varepsilon_0 {k_B}^2 T^2}$.

As depicted in Figure 1a, photogenerated excitons coexist with free charge carriers via the formation and dissociation processes described above. Both excitons and free carriers can recombine into the ground state and drift and diffuse to other locations. To determine the densities of free electrons (n), free holes (p), and excitons (n_{ex}), one needs to solve the electrostatic and continuity equations

$$\nabla\cdot\vec{E} = e(p + N_d - n - N_a)/\varepsilon_r\varepsilon_0 \tag{5}$$

$$\frac{dn}{dt} = k_d(E)n_{ex} - k_r np - R_{SRH} - \nabla\cdot\vec{J_n} \tag{6}$$

$$\frac{dp}{dt} = k_d(E)n_{ex} - k_r np - R_{SRH} - \nabla\cdot\vec{J_p} \tag{7}$$

$$\frac{dn_{ex}}{dt} = G_{ex} + k_r np - k_d(E)n_{ex} - n_{ex}/\tau_{ex} - \nabla\cdot\vec{J}_{ex} \tag{8}$$

where N_a is the acceptor concentration, N_d is the donor concentration, G_{ex} is the photoexcitation rate, and τ_{ex} is the lifetime of excitons. G_{ex} in eq 8 is set to initially generate excitons. We note that the simulation results do not change if photoexcitation initially generates free carriers. The simulated photocurrent distributions and photocurrent decay lengths remain the same if G_{ex} is moved to eqs 6 and 7 as shown in Figure S1b. This is because the excitons and free carriers quickly reach a balance through the fast pairing and dissociation process, regardless of whether excitons or free carriers are generated initially. Furthermore, higher-order terms such as Auger recombination may have impacts on the diffusion length as observed in WS_2 monolayers.[30] However, we do not consider that in this work as we used a relatively low laser power and did not observe an increase in diffusion lengths at higher laser powers in our previous experiments.[16] At a high laser intensity, bimolecular recombination may lead to a reduced effective carrier lifetime. For the sake of simplicity, we also ignore this effect. We assume that free carriers recombine through the Shockley–Read–Hall process at a rate R_{SRH}

$$R_{SRH} = \frac{np - {n_i}^2}{\tau_p(n + n_i) + \tau_n(p + n_i)} \tag{9}$$

where $\vec{J}_n$, $\vec{J}_p$, and $\vec{J}_{ex}$ are number (not charge) current densities of electrons, holes, and excitons, respectively. Each current density has both diffusion and drift components. Explicitly, we have

$$\vec{J_n} = -\mu_n n\vec{E} - \mu_n k_B T\nabla n/e \tag{10}$$

$$\vec{J_p} = \mu_p p\vec{E} - \mu_p k_B T\nabla p/e \tag{11}$$

$$\vec{J}_{ex} = -\mu_{ex} k_B T\nabla n_{ex}/e \tag{12}$$

where μ_n, μ_p, and μ_{ex} are the mobilities of electrons, holes, and excitons, respectively. We assume the Einstein relation is held in all three cases (for example, the diffusivity of excitons is $D_{ex} = \mu_{ex}k_B T/e$). The drift term in exciton current is absent because excitons are charge neutral. We ignore the photo-induced thermoelectric current as the observed photocurrent is much larger than that expected from such an effect,[16] confirmed by previous simulation work.[23,24]

The equations presented above can only be solved analytically by making some extreme assumptions. Though these assumptions are perhaps oversimplified, the analytic solutions can help improve our understanding of the physical mechanisms. We will consider three different assumptions below.

First, we consider that the material is under homogeneous photoexcitation. In this case, free carriers and excitons are uniformly distributed so all currents are zero. In addition, carrier pairing rate k_r is estimated to be 10^{-5} cm^3 s^{-1} using a mobility of 100 cm^2 V^{-1} s^{-1}, corresponding to a pairing time $\tau_{pair} = \frac{1}{k_r n}$ of a few picoseconds for $n = 10^{16}$ cm^{-3}. This is much faster than the carrier recombination with a time scale of 100 ns. Thus, we can also drop the n_{ex}/τ_{ex} term in eq 8. In the absence of an electric field, this then becomes an equilibrium equation

$$np/n_{ex} = K(0) = \frac{3}{4\pi {a_{ex}}^3} e^{-E_b/k_B T} \tag{13}$$

This equation describes the ratio of the free carrier densities over the exciton density in pseudoequilibrium. We shall see that this relation is held quite precisely even under inhomogeneous photoexcitation, as confirmed by the simulation results shown below. We also note that the equation presented above is similar in form to the Saha–Langmuir equation,[20,31] with the thermal de Broglie wavelength [$\lambda = h/\sqrt{2\pi m^*_{ex} k_B T}$, where $m^*_{ex} = m_e m_h/(m_e + m_h)$ is the effective mass of an exciton] replaced by exciton size a_{ex}. Both the Saha–Langmuir equation and eq 13 have been used to relate the exciton and free carrier densities in equilibrium.[20,21,28,32] Here we choose to use eq 13. As λ and a_{ex} are on the same order of magnitude, this choice is not expected to change our qualitative conclusions. More exactly in $MAPbI_3$, λ is estimated to be 5 times larger than a_{ex} at 300 K and 10 times larger at 50 K. As a result, the Saha model predicts an exciton fraction larger than that predicted from the Langevin model. Understanding this interesting discrepancy requires further theoretical and experimental work and is beyond the scope of this work.

Second, we consider a point photoexcitation source but assume that exciton density is negligibly small when $E_b \ll k_B T$. In this case, eqs 6 and 7 are reduced to the continuity equations for free carriers alone. One can show[22] that the photocurrent decays exponentially as the point photoexcitation is moved away from the contact ($I = I_0 e^{-x/L_d}$), with a decay

https://doi.org/10.1021/acs.jpclett.1c00507
J. Phys. Chem. Lett. 2021, 12, 3951−3959

length that equals the minority carrier diffusion length, for example, $L_d = \sqrt{D_p \tau_p}$ in n-type semiconductors.

Third, a more interesting assumption is that excitons are much more mobile than free carriers ($\mu_n \ll \mu_{ex}$, and $\mu_p \ll \mu_{ex}$) as indicated in our previous work.[16] In this extreme case, we can ignore the drift and diffusion of free carriers ($J_n = J_p = 0$). To simplify the discussion, we can assume the material is n-type and hence $R_{SRH} = p/\tau_p$ at low photoexcitation intensities. Considering a steady state in which the carrier concentration is independent of time, summing eqs 7 and 8 yields

$$\nabla \cdot \vec{J}_{ex} = G_{ex} - n_{ex}/\tau_{ex} - p/\tau_p \tag{14}$$

In the region outside the photoexcitation point, $G_{ex} = 0$ and the above equation in one dimension becomes

$$D_{ex}\frac{d^2 n_{ex}}{dx^2} = n_{ex}/\tau_{ex} + p/\tau_p \tag{15}$$

If we can further assume free carriers and excitons reach a dynamic balance at any position, we can use eq 13 to eliminate p. In addition, $n \approx N_d$ is expected to be uniform under low photoexcitation in n-type devices, so we have

$$D_{ex}\frac{d^2 n_{ex}}{dx^2} = n_{ex}[1/\tau_{ex} + K(0)/N_d\tau_p] = n_{ex}/\tau_{eff} \tag{16}$$

where τ_{eff} is the effective lifetime. The solution to this equation is a simple exponential distribution of exciton concentration, indicating that the photocurrent exponentially decays with a decay length that is determined by the exciton diffusion coefficient and a hybrid effective lifetime

$$L_d = \sqrt{D_{ex}\tau_{eff}} = \sqrt{\frac{D_{ex}}{1/\tau_{ex} + K(0)/N_d\tau_p}} \tag{17}$$

We carry out numerical simulation by a finite-element method to more rigorously solve the differential equations. We consider a device configuration similar to that in our previous experimental work,[16] where a microribbon of $MAPbI_3$ is in contact with two Au electrodes. A Gaussian distribution $\left\{ G_{ex} = G_0 \exp\left[-\frac{(x-x_0)^2}{2\sigma^2}\right] \right\}$ is assumed for the photoexcitation induced by the focused laser beam, where G_0 is the maximum carrier generation rate, x_0 is the laser center position, and σ is the Gaussian width. Because the CW laser scans slowly (a line scan takes ~1 s), a steady state can be assumed. We focus on devices with Schottky junctions at the $MAPbI_3$ and Au interface, as experimentally shown.[16,25] The typical size of the microribbon is tens of micrometers long, 1 μm thick, and 1 μm wide. As the longitudinal dimension is much larger than the lateral dimension in these microstructures, the three-dimensional (3D) charge transport can be simulated by 1D equations. The photoexcitation absorbed near the top of the microribbon (typically within the optical absorption depth of tens of nanometers) and the bottom gate may create inhomogeneous carrier distributions. However, even with such inhomogeneity, the 3D carrier transport can be simplified into one dimension, because the carriers flow parallel to the channel in most of the transport path in the device channel as previously shown.[23]

The device configuration used in the simulation was slightly different from our previous experimental setup[16] because 1D simulation does not allow for extraction of the photocurrent distributions outside the source-drain channel. Instead, the device was composed of a 1D channel between source and drain contacts as shown in Figure 1b, where we can still extract the carrier diffusion lengths from the photocurrent decay inside the channel to compare with our previous experimental results. To ensure the nature of diffusion, a zero source-drain bias was used in the simulation. A relatively large, 600 μm channel was used for the accurate extraction of the long photocurrent decay length at low temperatures.[24]

All physical parameters used in the simulation were chosen to represent the realistic experimental conditions and the $MAPbI_3$ microribbon properties.[16] We assumed an n-type channel with a donor concentration of $N_d = 5 \times 10^{16}$ cm^{-3} by default. The gate effect was considered by directly changing N_d. Schottky junctions with a barrier height $q\Phi_B = 0.35$ eV were used for both contacts, similar to that in real devices. At the metal contacts, we assume that the recombination occurs very fast, such that an equilibrium is reached. As a result, both the quasi-Fermi levels of free electrons and holes are equal to the work function of the metal, and free carriers and excitons reach equilibrium, i.e., $np/n_{ex} = K(E_m)$, where E_m is the electric field at the metal contact and is estimated from the abrupt Schottky junction equation. Both measured and calculated values of exciton binding energies in $MAPbI_3$ have been reported in a broad range from a few millielectronvolts to >50 meV.[33] However, it is largely agreed that the binding energy of excitons is considerably larger in the low-temperature crystal phase. The exciton binding energy values used in our simulation were chosen to be 10 meV for the tetragonal phase and 20−30 meV for the orthorhombic phase below a T_c of 160 K, consistent with the typical values in previous reports.[34] The justification of values for dielectric constants and exciton size can be found in ref 16. We set the exciton mobility to be ~300 times that for free carriers, and their values were chosen to match our experimental results. We chose temperature-dependent mobilities for both free carriers and excitons ($\mu \sim T^{-3/2}$), assuming phonon scattering is dominant.[10,35] Lifetimes of free carriers and excitons were chosen to have a similar power law dependence ($\tau \sim T^{-3/2}$).[36] We note that the simulation results are robust against the details of the power law dependence of mobilities and lifetimes, because the dominant factor governing the temperature-dependent diffusion length is the exciton fraction that exponentially depends on T. The simulated diffusion length is similar when using a T-independent lifetime (Figure S2). Simulation parameters are listed in Table 1.

Python with a SciPy library was used as a differential equation solver. Non-uniform mesh sizes were used, with a high-resolution 3 nm mesh size near the metal−semiconductor junctions and the laser injection position, and gradually increasing mesh sizes to a few hundred nanometers at places where carrier concentrations slowly varied. We confirmed that simulations using finer mesh did not show notable changes. We further cross-checked the Python simulation results with COMSOL Multiphysics, a commercial finite element solver. The two methods generated highly consistent results as shown in Figure S1c. We chose to mainly use Python because of its flexibility.

We first present the simulated distributions of the electric field, free charge carriers, and excitons at 300 and 80 K (Figure 1). We set the source-drain bias to zero ($V_{sd} = 0$ V) and fix the focused laser position at 10 μm from the left contact. The laser intensity is sufficiently weak, and the photoexcited electron

https://doi.org/10.1021/acs.jpclett.1c00507
J. Phys. Chem. Lett. 2021, 12, 3951−3959

Table 1. Simulation Parameters

symbol	physical meaning	value
E_g	bandgap	1.61 eV
N_d	donor concentration	5×10^{16} cm^{-3}
N_A	acceptor concentration	0
$q\Phi_B$	Schottky barrier height	0.35 eV
ε_r	dielectric constant	30.4 ($T \geq 160$ K)
		25.7 ($T \leq 160$ K)
a_{ex}	exciton size	3.37 nm ($T \geq 160$ K)
		2.95 nm ($T \leq 160$ K)
E_b	exciton binding energy	10 meV ($T \geq 160$ K)
		20 or 30 meV ($T \leq 160$ K)
m_e	electron effective mass	0.19 m_0
m_h	hole effective mass	0.23 m_0
μ_n	electron mobility	$96.6 \times (300/T)^{3/2}$ cm^2 V^{-1} s^{-1}
μ_p	hole mobility	$96.6 \times (300/T)^{3/2}$ cm^2 V^{-1} s^{-1}
μ_{ex}	exciton mobility	$27482 \times (300/T)^{3/2}$ cm^2 V^{-1} s^{-1}
τ_n	electron lifetime	$100 \times (300/T)^{3/2}$ ns
τ_p	hole lifetime	$100 \times (300/T)^{3/2}$ ns
τ_{ex}	exciton lifetime	$1000 \times (300/T)^{3/2}$ ns
L	channel length	600 μm
A_z	cross-section area	0.4 μm^2
λ	laser wavelength	532 nm
σ	laser beam width	200 nm

(majority carrier) density is much lower than that in the dark; therefore, the electronic band bending is not perturbed by the light. The electric field is only large in the Schottky junction near the contact, reaching 3 V/μm (Figure 1c). The electric field is slightly smaller at low temperatures, likely because of the reduced effective densities of states (N_c and N_v). This electric field is on the same order of magnitude as that needed to split excitons, which can be estimated by E_b/qa_{ex}.

The simulation allows us to visualize the distributions of the free hole (minority carrier) density (p) and exciton density (n_{ex}). Both peaked at the laser excitation position and decay much more slowly at low temperatures, indicating more efficient diffusion (Figure 1d,e). Both p and n_{ex} decrease to zero at the contact as enforced by the boundary condition of an infinite recombination rate. Because the photoexcited free hole density is much larger than the dark hole density ($\Delta p \gg p_0$) as under the experimental condition, the free hole density is almost all from photoexcitation ($p \approx \Delta p$). We can then use the ratio $f_{ex} = n_{ex}/(n_{ex} + p)$ to evaluate the fraction of excitons over the total photoexcited carriers. f_{ex} ranges from 0 to 1, where 1 means that photoexcitation produces only excitons. Though both p and n_{ex} change significantly in the channel, the distribution of f_{ex} is uniform in the electric field free zone (Figure 1f). This is because coexisting excitons and free carriers reach a dynamical balance governed by eq 13. This balance is not affected by the diffusion and recombination of photoexcited carriers, as both the formation and dissociation rates of excitons are much faster than the diffusion and recombination processes, as confirmed by simulation (Figures S4 and S5). We also note that the exciton formation rate is estimated by the classical Langevin recombination (eq 1) in this work. A more rigorous treatment that considers phonon interactions yields a similar or slightly slower exciton formation rate of up to tens of picoseconds.[37] This is still much faster than the carrier recombination and transport process, and hence, our conclusion that excitons and free carriers reach a balance still holds. In the field free region, f_{ex} increases from 1%

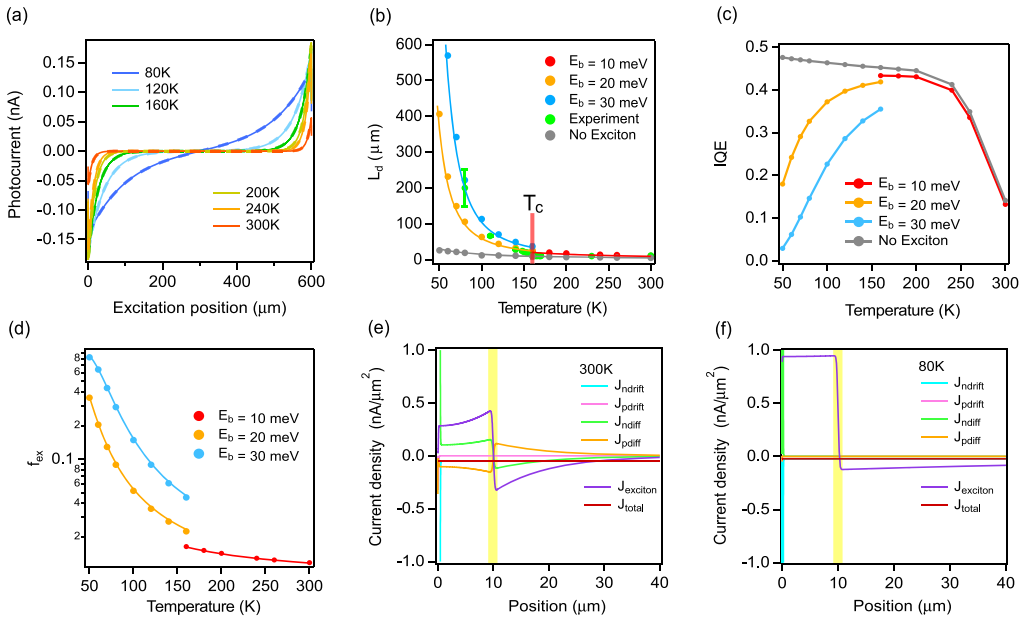

Figure 2. Simulated temperature-dependent photocurrent distributions in a $MAPbI_3$ microribbon device. (a) Photocurrent as a function of the photoexcitation location at various temperatures using an E_b of 20 meV below T_c and an E_b of 10 meV above T_c. The solid lines are simulated values, and the dashed lines are the fitting by a hyperbolic function. (b) Temperature-dependent L_d at different E_b values or in the absence of excitons. The circles are L_d values extracted from the hyperbolic fitting of photocurrent distributions as in panel a. The solid curves are calculated using eq 17. The experimental results (green circles, extracted from ref 16) are also shown to compare with the simulation. A semilog plot is shown in Figure S6. (c) IQE at the photocurrent peak as a function of T. (d) f_{ex} in the electric field free region as a function of T. The circles are extracted from the simulation, and the solid curves are calculated using eq 13. (e and f) Distributions of current density components at 300 and 80 K, respectively. The vertical yellow lines indicate the photoexcitation positions.

https://doi.org/10.1021/acs.jpclett.1c00507
J. Phys. Chem. Lett. 2021, 12, 3951−3959

at 300 K to 9% at 80 K. The reduced f_{ex} in the depletion region is caused by the exciton splitting under the strong electric field.

Next, we simulate the photocurrent as a function of the photoexcitation position at V_{sd} = 0 V and across various temperatures. The photocurrent decays rapidly as the photoexcitation position moves away from the contact in the high-temperature phase with an E_b of 10 meV. Below the transition temperature (T_c = 160 K) when E_b increases, the decay is much slower (Figure 2a,b). Above the T_c, the photocurrent decay follows very well an exponential function, from which decay length L_d can be extracted. L_d only slightly increases from 10 to 20 μm when T is reduced from 300 to 160 K. The values of L_d are very close to those expected from free minority carrier diffusion, indicating exciton diffusion makes a negligible contribution to photocurrent at these temperatures. This is consistent with the E_b being significantly below k_BT for the high-temperature phase. L_d then jumps from 20 to 30 μm for an E_b of 20 meV (40 μm for an E_b of 30 meV) as T drops below T_c (Figure 2b and Figure S6), caused by the sudden increase in E_b.

At low T, the photocurrent decays slowly and its profiles substantially deviate from a single-exponential function, due to the decay length becoming comparable to the channel length. To accurately extract the decay length, we fit the curve with a hyperbolic function $I(x_0) = A \sinh \frac{x_0 - L/2}{L_d}$, where L = 600 μm is the channel length and A and L_d are fitting parameters. The photocurrent distributions can be fit very well by this function. The hyperbolic fitting can be justified by considering the continuity equation and boundary conditions (see details in the Supporting Information).

As T is reduced from 160 to 50 K, L_d extracted from the simulated photocurrent profiles increases sharply, by 11 times for an E_b of 20 meV and 25 times for an E_b of 30 meV. If excitons are not considered, L_d increases by only ~3-fold (Figure 2b). This comparison signals the importance of the exciton contribution to the overall carrier diffusion length. The simulated T-dependent L_d, both the sudden jump across the phase transition and the rapid increase below T_c, agrees very well with our previous experimental results, which are also plotted in Figure 2b. The simulated f_{ex} is close to zero above T_c and reaches ~40% for an E_b of 20 meV and 80% for an E_b of 30 meV at 50 K (Figure 2d).

Remarkably, both L_d and f_{ex} are also in excellent agreement with that calculated from eqs 17 and 13, respectively, as shown in panels b and d of Figure 3 (solid lines are calculated curves, and circles are simulated). This indicates that the assumptions made when deriving these equations, including (1) excitons and free carriers reaching a dynamic balance across the channel and (2) neglecting the free carrier current, are reasonable. These analytic expressions provide not only a simple method for estimating the L_d and f_{ex} values but also a clear and intuitive picture of understanding the transport of photoexcited carriers. Though excitons and free carriers are set to have very different mobilities and lifetimes, their simulated distributions (Figure 1) and photocurrent profiles (Figure 2a) clearly follow an exponential (or hyperbolic) function with only one characteristic decay length (L_d), instead of having multiple components (such as $\sqrt{D_p\tau_p}$ and $\sqrt{D_{ex}\tau_{ex}}$). This is because free carriers and excitons convert into each other frequently through a picosecond pairing/dissociation process and hence reach a pseudoequilibrium with a uniform exciton fraction along the device channel (except at the Schottky junction). As a result,

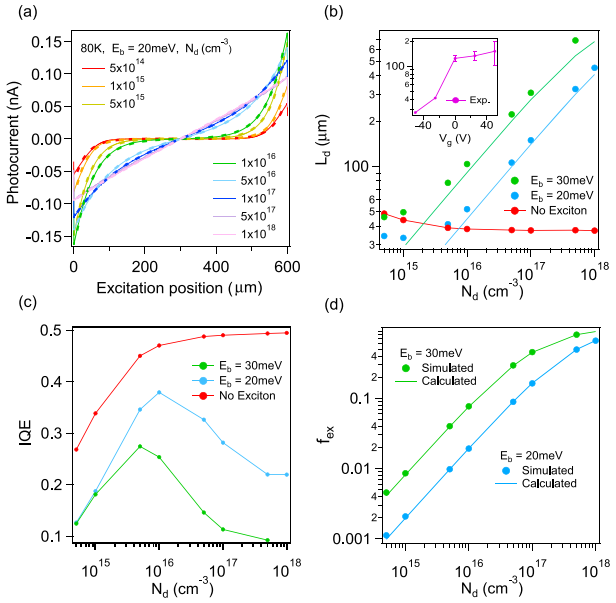

Figure 3. Simulated doping level-dependent photocurrent distributions in a $MAPbI_3$ microribbon device at 80 K. (a) Photocurrent as a function of photoexcitation location with various donor concentrations for an E_b of 20 meV below T_c. The photocurrent distributions for an E_b of 30 meV are shown in Figure S9. The hyperbolic fittings for extracting L_d are shown as dashed lines. (b) Donor concentration-dependent L_d at different values of E_b or in the absence of excitons. The circles are L_d values extracted from the hyperbolic fitting of the simulated photocurrent distributions as in panel a. The solid curves are calculated using eq 17. The inset shows the experimental result from ref 16. (c) Simulated IQE at the photocurrent peak position as a function of donor concentration. (d) Simulated exciton fraction (circles) in the electric field free zone. The expected f_{ex} values calculated by eq 13 are shown as solid lines.

the coexisting free carriers and excitons can be regarded as one species moving at the much higher exciton mobility but with a hybrid lifetime as in eq 17.

The internal quantum efficiency (IQE), defined as the ratio of electrons collected to photons absorbed in the microribbon, is calculated at the maximum current position and plotted against T (Figure 2c). The simulated IQE first increases when T is reduced from 300 to ~250 K and then saturates at ~40%. Such an IQE increase is caused by the channel resistance (R) decreasing at lower values of T. As carrier mobility is assumed to increase at lower values of T, R decreases, resulting in an increased IQE. This explanation is confirmed by the simulation results for a shorter channel device as shown in Figure S7. The 40% IQE (instead of the ideal 50% value for the device with two Schottky contacts) is also caused by the series channel resistance.[23] If exciton formation is not considered, the simulated IQE remains high below T_c. In this case, IQE slightly increases closer to 50% as R decreases at lower values of T, but when exciton formation is considered, IQE significantly decreases at lower values of T and drops to 18% for an E_b of 20 meV and 3% for an E_b of 30 meV at 50 K. This is because the equilibrium constant of exciton dissociation $K(E)$ depends on T as shown in eqs 4 and 13. $K(E)$ is reduced by more than 1 order of magnitude at low values of T as shown in Figure S8. The reduced photocurrent efficiency at lower values of T is consistent with previous experimental work.[38]

https://doi.org/10.1021/acs.jpclett.1c00507
J. Phys. Chem. Lett. 2021, 12, 3951−3959

To better understand photocurrent generation, we plot the simulated distributions of individual photocurrent components when the photoexcitation is fixed at $x = 10$ μm at 300 and 80 K (Figure 2e,f). The total current is the sum of four components, including electron drift, electron diffusion, hole drift, and hole diffusion. Though each component varies along the channel, the total current must be uniform because of charge continuity as shown in the plot. In comparison, we also plot the exciton diffusion current (eJ_{ex}) as defined in eq 12. Exciton flow does not directly generate electric current because excitons are charge neutral, but excitons can be split into electrons and holes under the electric field in the Schottky junction, where the efficient charge separation can produce photocurrent. As shown clearly in the figure, the exciton current at 80 K is much higher than that at 300 K, because more excitons are formed with increased exciton binding energy. At 80 K, the exciton current is much larger than free carrier diffusion/drift components, indicating the exciton flow dominates photocurrent generation.

To compare with the experimentally measured gate-dependent L_d, we simulate photocurrent distributions with various N_d values at 80 K, as both doping and gate can change the Fermi level. If only free carriers are considered, the simulated L_d values remain approximately the same in a large range of N_d values (Figure 3b), inconsistent with the experimental results that L_d changes by a factor of 8 under gate (Figure 3b, inset).[16] The slight increase in L_d at low N_d values is caused by the longer SRH recombination lifetime at a low doping density (eq 9). On the contrary, if excitons are considered, the simulated photocurrent decays much more slowly as N_d increases (Figure 3a,b), which is consistent with the experimental results. The simulation again agrees well with eq 17, except at very low values of N_d, because the n-type assumption no longer holds at such low doping concentrations. A higher N_d, and hence a higher electron density, increases the probability of exciton formation, leading to a larger exciton fraction as shown in eq 13. The larger f_{ex} is confirmed directly by simulation and agrees well with the calculation by eq 13 (Figure 3d). The simulated peak IQE drops at a higher N_d (Figure 3c), presumably because the excitons are less likely to split after reaching the contact due to a larger exciton fraction and smaller contact band bending. IQE also drops at lower values of N_d because of a more resistive channel. We note that at high N_d values or a high laser intensity, E_b may be reduced because of strong field screening.[39] This effect is not considered in our simulation.

Photon recycling via re-absorption of emitted photons by the material has been proposed as a possible mechanism for extending the propagation of photoexcitation energy.[40] We now consider this effect using numerical simulation. To account for this effect, we add an internal generation term in the continuity equations (eqs 6 and 7) in addition to the external generation term by laser, similar to the previous work[41]

$$G_{int} = k_{rad} n p p_r \tag{18}$$

where k_{rad} is the radiative recombination coefficient and p_r is the re-absorption probability. We take p_r to be 0.9 and k_{rad} to be $2 \times 10^{-10} \times (T/300)^{3/2}$ cm^3/s, which corresponds to a radiative lifetime that equals the minority carrier lifetime used in SRH recombination ($\tau_{rad} = \tau_p$) at any temperature. We turn off the exciton effect by letting $k_d(E)$ and k_r be zero in eqs 6 and 7 and add a radiative recombination term. The new hole continuity equation in the steady state then becomes

$$G_{ex} + G_{int} - k_{rad} n p - R_{SRH} - \nabla \cdot \vec{J}_p = 0 \tag{19}$$

The electron continuity equation is similar, but $\vec{J}_p$ is replaced by $\vec{J}_n$. The simulated photocurrent distributions when considering photon recycling effects show an increase in L_d of ~40% (Figure 4b). This result indicates that while photon recycling certainly can have an effect on modifying L_d, the major contribution to the experimentally observed much longer L_d is likely not from this effect. Equation 19 can be simplified under the reasonable assumptions that photocurrent is dominated by minority carrier diffusion and the photoexcitation intensity is low so that $n = N_d$. In the region outside of photoexcitation of a 1D channel that is free of electric field, the equation becomes

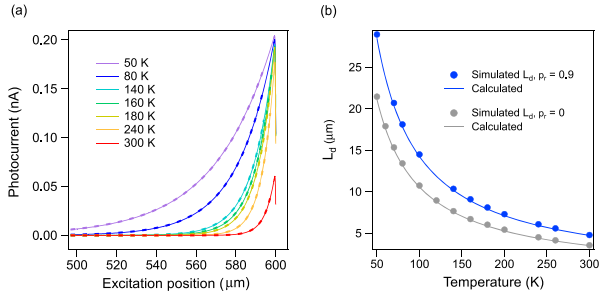

Figure 4. Simulated photocurrent distributions to take into account photon recycling effects in a $MAPbI_3$ microribbon device. (a) Simulated photocurrent profiles through a range of temperatures both below and above T_c for a p_r of 0.9. Each curve is fitted with an exponential function, shown as a dashed line overlaying the corresponding curve. To clearly demonstrate the fitting quality, we show the photocurrent distributions only near the right contact. The left contact mirrors the right but with the opposite current polarity. (b) Diffusion length L_d as a function of temperature for the baseline p_r of 0 (in the absence of photon recycling) and for a p_r of 0.9. The circles are L_d values extracted from the hyperbolic fitting of the simulated photocurrent distributions as in panel a. The solid curves are calculated using eq 21.

$$D_p \frac{d^2 p}{dx^2} = [1/\tau_p + (1 - p_r)/\tau_{rad}]p \tag{20}$$

This leads to an exponential photocurrent with a decay length given by

$$L_d = \sqrt{\frac{D_p}{1/\tau_p + (1 - p_r)/\tau_{rad}}} \tag{21}$$

The simulated photocurrent decay lengths are consistent with this expression as shown in Figure 4b.

In summary, we have performed rigorous finite-element simulations to model the transport of coexisting excitons and free carriers locally excited by a focused laser. The device modeling shows that highly mobile excitons become important and dominate the photocurrent decay profiles at low temperatures in halide perovskites. Our simulations are highly consistent with our previous experimental results.[16] The main conclusions are as follows. (1) the effective diffusion length of photogenerated carriers, as evaluated by the simulated

https://doi.org/10.1021/acs.jpclett.1c00507
J. Phys. Chem. Lett. 2021, 12, 3951−3959

photocurrent decay length in SPCM, rapidly increases below the phase transition temperature (Figure 2). The simulated L_d increases much faster than expected from phonon scattering of free carriers, due to the exponentially increased fraction of highly mobile excitons at lower temperatures. (2) The diffusion length increases at higher doping levels as the higher majority carrier concentration promotes the formation of excitons (Figure 3). (3) The temperature and doping level-dependent photocurrent decay lengths both agree quite well with the analytic result expressed in eq 17, which is derived under the assumption that excitons and free carriers reach a dynamic balance and hence the exciton fraction remains constant through the device channel. (4) The photocurrent quantum efficiency can be tuned by temperature and doping level. The decrease in efficiency at low temperatures or at high doping levels can be understood by the difficulty of exciton splitting. (5) The simulated photon recycling effects based on internal re-absorption do not appear to generate a sufficient increase in the decay length to explain the experimental results. Our work sets up a rigorous simulation method for understanding the role of excitons in the transport of photogenerated carriers. The simulation also provides a more accurate interpretation of the experimental results obtained from a widely used spatially resolved optoelectronic technique. We expect this modeling method to be used in a variety of materials beyond halide perovskites, such as two-dimensional materials with a large excitonic binding energy.

■ ASSOCIATED CONTENT

Supporting Information

The Supporting Information is available free of charge at https://pubs.acs.org/doi/10.1021/acs.jpclett.1c00507.

Analytic justification of extraction of the carrier diffusion length by hyperbolic fittings; comparison of simulation results by Python and COMSOL; comparison of simulation results by initial generation of excitons or free carriers; simulated photocurrent decay lengths with temperature-independent lifetimes; simulated distributions of electric field, free electron, hole, and exciton densities across the entire channel; comparison of rates for the exciton pairing, dissociation, transport, and recombination processes at 80 and 300 K; semilog plot of the simulated photocurrent decay length as a function of temperature; simulated peak internal quantum efficiency in a shorter channel device; equilibrium constant of exciton dissociation $K(E)$ as a function of temperature; and photocurrent distributions at various doping levels simulated by using an excitonic binding energy of 30 meV (PDF)

■ AUTHOR INFORMATION

Corresponding Author

Dong Yu − *Department of Physics and Astronomy, University of California−Davis, Davis, California 95616, United States;* orcid.org/0000-0002-8386-065X; Email: yu@physics.ucdavis.edu

Authors

Kuen Wai Tang − *Department of Physics and Astronomy, University of California−Davis, Davis, California 95616, United States*

Senlei Li − *Department of Physics and Astronomy, University of California−Davis, Davis, California 95616, United States*

Spencer Weeden − *Department of Physics, Carleton College, Northfield, Minnesota 55057, United States*

Ziyi Song − *Department of Physics and Astronomy, University of California−Davis, Davis, California 95616, United States*

Luke McClintock − *Department of Physics and Astronomy, University of California−Davis, Davis, California 95616, United States*

Rui Xiao − *Department of Physics and Astronomy, University of California−Davis, Davis, California 95616, United States*

R. Tugrul Senger − *Department of Physics, Izmir Institute of Technology, 35430 Izmir, Turkey*

Complete contact information is available at: https://pubs.acs.org/10.1021/acs.jpclett.1c00507

Notes

The authors declare no competing financial interest.

■ ACKNOWLEDGMENTS

This work was supported by the National Science Foundation Grants DMR-1710737 and DMR-1838532. R.T.S. acknowledges the support from The Turkish Fulbright Commission Visiting Scholar Program.

■ REFERENCES

(1) You, Y.; Zhang, X.-X.; Berkelbach, T. C.; Hybertsen, M. S.; Reichman, D. R.; Heinz, T. F. Observation of biexcitons in monolayer WSe 2. *Nat. Phys.* **2015**, *11*, 477−481.

(2) Makarov, N. S.; Guo, S.; Isaienko, O.; Liu, W.; Robel, I.; Klimov, V. I. Spectral and dynamical properties of single excitons, biexcitons, and trions in cesium-lead-halide perovskite quantum dots. *Nano Lett.* **2016**, *16*, 2349−2362.

(3) Neukirch, A. J.; Nie, W.; Blancon, J.-C.; Appavoo, K.; Tsai, H.; Sfeir, M. Y.; Katan, C.; Pedesseau, L.; Even, J.; Crochet, J. J.; et al. Polaron stabilization by cooperative lattice distortion and cation rotations in hybrid perovskite materials. *Nano Lett.* **2016**, *16*, 3809−3816.

(4) Su, R.; Diederichs, C.; Wang, J.; Liew, T. C.; Zhao, J.; Liu, S.; Xu, W.; Chen, Z.; Xiong, Q. Room-temperature polariton lasing in all-inorganic perovskite nanoplatelets. *Nano Lett.* **2017**, *17*, 3982−3988.

(5) Stern, M.; Umansky, V.; Bar-Joseph, I. Exciton liquid in coupled quantum wells. *Science* **2014**, *343*, 55−57.

(6) High, A. A.; Leonard, J. R.; Hammack, A. T.; Fogler, M. M.; Butov, L. V.; Kavokin, A. V.; Campman, K. L.; Gossard, A. C. Spontaneous coherence in a cold exciton gas. *Nature* **2012**, *483*, 584−588.

(7) Hou, Y.; Wang, R.; Xiao, R.; McClintock, L.; Clark Travaglini, H.; Paulus Francia, J.; Fetsch, H.; Erten, O.; Savrasov, S. Y.; Wang, B.; et al. Millimetre-long transport of photogenerated carriers in topological insulators. *Nat. Commun.* **2019**, *10*, 5723.

(8) Williams, R.; Song, K. The self-trapped exciton. *J. Phys. Chem. Solids* **1990**, *51*, 679−716.

(9) Yuan, Z.; Zhou, C.; Tian, Y.; Shu, Y.; Messier, J.; Wang, J. C.; Van De Burgt, L. J.; Kountouriotis, K.; Xin, Y.; Holt, E.; et al. One-dimensional organic lead halide perovskites with efficient bluish white-light emission. *Nat. Commun.* **2017**, *8*, 14051.

(10) Tamor, M.; Wolfe, J. Drift and diffusion of free excitons in Si. *Phys. Rev. Lett.* **1980**, *44*, 1703.

(11) Rakita, Y.; Cohen, S. R.; Kedem, N. K.; Hodes, G.; Cahen, D. Mechanical properties of APbX 3 (A = Cs or CH 3 NH 3; X = I or Br) perovskite single crystals. *MRS Commun.* **2015**, *5*, 623−629.

(12) Sendner, M.; Nayak, P. K.; Egger, D. A.; Beck, S.; Müller, C.; Epding, B.; Kowalsky, W.; Kronik, L.; Snaith, H. J.; Pucci, A.; et al. Optical phonons in methylammonium lead halide perovskites and implications for charge transport. *Mater. Horiz.* **2016**, *3*, 613−620.

(13) Devreese, J. T.; Alexandrov, A. S. Fröhlich polaron and bipolaron: recent developments. *Rep. Prog. Phys.* **2009**, *72*, 066501.
(14) Miyata, K.; Atallah, T. L.; Zhu, X.-Y. Lead halide perovskites: Crystal-liquid duality, phonon glass electron crystals, and large polaron formation. *Sci. Adv.* **2017**, *3*, e1701469.
(15) Wright, A. D.; Verdi, C.; Milot, R. L.; Eperon, G. E.; Pérez-Osorio, M. A.; Snaith, H. J.; Giustino, F.; Johnston, M. B.; Herz, L. M. Electron-phonon coupling in hybrid lead halide perovskites. *Nat. Commun.* **2016**, *7*, 11755.
(16) McClintock, L.; Xiao, R.; Hou, Y.; Gibson, C.; Travaglini, H. C.; Abramovitch, D.; Tan, L. Z.; Senger, R. T.; Fu, Y.; Jin, S.; et al. Temperature and gate dependence of carrier diffusion in single crystal methylammonium lead iodide perovskite microstructures. *J. Phys. Chem. Lett.* **2020**, *11*, 1000−1006.
(17) Merzbacher, E. *Quantum Mechanics*, 3rd ed.; John Wiley Sons, Inc.: New York, 1998; p 462.
(18) Pollmann, J.; Büttner, H. Effective Hamiltonians and binding energies of Wannier excitons in polar semiconductors. *Phys. Rev. B* **1977**, *16*, 4480−4490.
(19) Senger, R. T.; Bajaj, K. K. Optical properties of confined polaronic excitons in spherical ionic quantum dots. *Phys. Rev. B: Condens. Matter Mater. Phys.* **2003**, *68*, 045313.
(20) D'innocenzo, V.; Grancini, G.; Alcocer, M. J.; Kandada, A. R. S.; Stranks, S. D.; Lee, M. M.; Lanzani, G.; Snaith, H. J.; Petrozza, A. Excitons versus free charges in organo-lead tri-halide perovskites. *Nat. Commun.* **2014**, *5*, 3586.
(21) Häusermann, R.; Knapp, E.; Moos, M.; Reinke, N. A.; Flatz, T.; Ruhstaller, B. Coupled optoelectronic simulation of organic bulk-heterojunction solar cells: Parameter extraction and sensitivity analysis. *J. Appl. Phys.* **2009**, *106*, 104507.
(22) Graham, R.; Yu, D. Scanning photocurrent microscopy in semiconductor nanostructures. *Mod. Phys. Lett. B* **2013**, *27*, 1330018.
(23) Xiao, R.; Hou, Y.; Law, M.; Yu, D. On the use of photocurrent imaging to determine carrier diffusion lengths in nanostructured thin-film field-effect transistors. *J. Phys. Chem. C* **2018**, *122*, 18356−18364.
(24) Fu, D.; Zou, J.; Wang, K.; Zhang, R.; Yu, D.; Wu, J. Electrothermal dynamics of semiconductor nanowires under local carrier modulation. *Nano Lett.* **2011**, *11*, 3809−3815.
(25) Xiao, R.; Hou, Y.; Fu, Y.; Peng, X.; Wang, Q.; Gonzalez, E.; Jin, S.; Yu, D. Photocurrent mapping in single-crystal methylammonium lead iodide perovskite nanostructures. *Nano Lett.* **2016**, *16*, 7710−7717.
(26) Semonin, O. E.; Elbaz, G. A.; Straus, D. B.; Hull, T. D.; Paley, D. W.; Van der Zande, A. M.; Hone, J. C.; Kymissis, I.; Kagan, C. R.; Roy, X.; et al. Limits of carrier diffusion in N-type and P-type CH3NH3PbI3 perovskite single crystals. *J. Phys. Chem. Lett.* **2016**, *7*, 3510−3518.
(27) Wang, X.; Ling, Y.; Chiu, Y.-C.; Du, Y.; Barreda, J. L.; Perez-Orive, F.; Ma, B.; Xiong, P.; Gao, H. Dynamic electronic junctions in organic-inorganic hybrid perovskites. *Nano Lett.* **2017**, *17*, 4831−4839.
(28) Braun, C. L. Electric field assisted dissociation of charge transfer states as a mechanism of photocarrier production. *J. Chem. Phys.* **1984**, *80*, 4157−4161.
(29) Fuoss, R.; Accascina, F. *Electrolytic conductance*; Interscience Publishers, 1959.
(30) Kulig, M.; Zipfel, J.; Nagler, P.; Blanter, S.; Schüller, C.; Korn, T.; Paradiso, N.; Glazov, M. M.; Chernikov, A. Exciton diffusion and halo effects in monolayer semiconductors. *Phys. Rev. Lett.* **2018**, *120*, 207401.
(31) Saha, M. N. On a physical theory of stellar spectra. *Proc. R. Soc. London, Ser. A* **1921**, *99*, 135−153.
(32) Mariano, F.; Cretí, A.; Carbone, L.; Genco, A.; D'Agostino, S.; Carallo, S.; Montagna, G.; Lomascolo, M.; Mazzeo, M. The enhancement of excitonic emission crossing Saha equilibrium in trap passivated CH3NH3PbBr3 perovskite. *Commun. Phys.* **2020**, *3*, 41.
(33) Baranowski, M.; Plochocka, P. Excitons in Metal-Halide Perovskites. *Adv. Energy Mater.* **2020**, *10*, 1903659.
(34) Jiang, Y.; Wang, X.; Pan, A. Properties of excitons and photogenerated charge carriers in metal halide perovskites. *Adv. Mater.* **2019**, *31*, 1806671.
(35) Frost, J. M. Calculating polaron mobility in halide perovskites. *Phys. Rev. B: Condens. Matter Mater. Phys.* **2017**, *96*, 195202.
(36) Schenk, A. A model for the field and temperature dependence of Shockley-Read-Hall lifetimes in silicon. *Solid-State Electron.* **1992**, *35*, 1585−1596.
(37) Piermarocchi, C.; Tassone, F.; Savona, V.; Quattropani, A.; Schwendimann, P. Exciton formation rates in GaAs/Al x Ga 1- x As quantum wells. *Phys. Rev. B: Condens. Matter Mater. Phys.* **1997**, *55*, 1333.
(38) Phuong, L. Q.; Nakaike, Y.; Wakamiya, A.; Kanemitsu, Y. Free excitons and exciton-phonon coupling in CH3NH3PbI3 single crystals revealed by photocurrent and photoluminescence measurements at low temperatures. *J. Phys. Chem. Lett.* **2016**, *7*, 4905−4910.
(39) Feneberg, M.; Osterburg, S.; Lange, K.; Lidig, C.; Garke, B.; Goldhahn, R.; Richter, E.; Netzel, C.; Neumann, M. D.; Esser, N.; et al. Band gap renormalization and Burstein-Moss effect in silicon- and germanium-doped wurtzite GaN up to 10^{20} cm^{-3}. *Phys. Rev. B: Condens. Matter Mater. Phys.* **2014**, *90*, 075203.
(40) Pazos-Outón, L. M.; Szumilo, M.; Lamboll, R.; Richter, J. M.; Crespo-Quesada, M.; Abdi-Jalebi, M.; Beeson, H. J.; Vrućinić, M.; Alsari, M.; Snaith, H. J.; et al. Photon recycling in lead iodide perovskite solar cells. *Science* **2016**, *351*, 1430−1433.
(41) Kirchartz, T.; Márquez, J. A.; Stolterfoht, M.; Unold, T. Photoluminescence-based characterization of halide perovskites for photovoltaics. *Adv. Energy Mater.* **2020**, *10*, 1904134.

https://doi.org/10.1021/acs.jpclett.1c00507
J. Phys. Chem. Lett. 2021, 12, 3951−3959